IEEE Access
Multidisciplinary | Rapid Review | Open Access Journal

Received May 30, 2019, accepted June 24, 2019, date of publication July 5, 2019, date of current version July 25, 2019.

Digital Object Identifier 10.1109/ACCESS.2019.2927053

Pedestrian Dead Reckoning Using Pocket-Worn Smartphone

HONGYU ZHAO[1,2], (Member, IEEE), LUYAO ZHANG[1,2], SEN QIU[1,2], (Member, IEEE), ZHELONG WANG[1,2], (Senior Member, IEEE), NING YANG[1,2], AND JIAN XU[3]

[1]Key Laboratory of Intelligent Control and Optimization for Industrial Equipment of Ministry of Education, Dalian University of Technology, Dalian 116024, China
[2]School of Control Science and Engineering, Dalian University of Technology, Dalian 116024, China
[3]Department of Physical Education, Dalian University of Technology, Dalian 116024, China

Corresponding author: Hongyu Zhao (zhaohy@dlut.edu.cn)

This work was supported in part by the China Postdoctoral Science Foundation under Grant 2017M621131 and Grant 2017M621132, in part by the National Natural Science Foundation of China under Grant 61873044 and Grant 61803072, in part by the Dalian Science and Technology Innovation Fund under Grant 2018J12SN077, in part by the National Defense Pre-Research Foundation under Grant 614250607011708, and in part by the Fundamental Research Funds for the Central Universities under Grant DUT18RC(4)036 and Grant DUT18RC(4)034.

ABSTRACT Indoor pedestrian dead reckoning (PDR) extends the location-based service (LBS) to environments, where GPS or beacon signals are degraded or unavailable. A practical PDR system should consider the absence of any infrastructure or prior knowledge of the environment. This paper presents a PDR system based on a pocket-worn smartphone, which tracks a person's location through dead reckoning calculation by using the sensors embedded in smartphones. However, a smartphone-based PDR system faces various challenges, especially the heading drift due to gyroscope bias. In this paper, the gradient descent algorithm (GDA) is improved to reduce the heading drift, by fusing inertial data with only a fraction of magnetometer data that are accurate and usable. There is an 80% probability that the heading error is reduced to less than 4 degrees. Besides, a stride detection method is developed based on thigh angles, and then, a stride length estimation method is implemented in a complementary way. The experiments were conducted along with three types of reference paths, and the experimental results demonstrate that the average position errors along the three paths are 1.62%, 1.00%, and 0.92%, respectively. Despite the inherent sensor noise and complex human locomotion, the smartphone-based PDR system has great potential in pedestrian tracking.

INDEX TERMS Indoor localization, pedestrian tracking, inertial sensors, sensor fusion, gait analysis.

I. INTRODUCTION

In the past decades, smartphones have gradually become indispensable electronic products in people's daily life [1]. Smartphone has a variety of built-in sensors, such as Wi-Fi, GPS, microphone, magnetometer, and inertial sensors (i.e., gyroscope and accelerometer). It is recommended to use their built-in sensors and computational units for pedestrian tracking. With the rapid development of smartphone technology and the growth in the number of smartphone users, smartphone-based navigation systems have proven valuable in many applications [2]. As people spend most of their time indoors (at work or at home), there is a need for an autonomous pedestrian navigation solution that can be applicable to indoor location-based services (LBS). Smartphone-based LBS using global navigation satellite system (GNSS) have bb3b3een widely used outdoors. Although, to a large extent, the problem of outdoor localization has been solved, there is no clear dominant technology for indoor localization, as the GNSS signals are degraded or denied indoors due to signal attenuation and multipath effects [3].

Many researches have focused on indoor pedestrian tracking [4], [5] based on body sensor networks (BSNs) [6]–[9]. Various data sources have been used for this purpose, such as wireless fidelity (Wi-Fi) [10], Bluetooth low energy (BLE) [11], ultra-wideband (UWB) [12], [13], radio frequency identification (RFID) [14], geomagnetic field [15], and inertial data [16], [17]. Among these schemes, inertial measurement units (IMUs) are preferable due to their self-contained nature. Micro-electro-mechanical-systems (MEMS)-based IMUs are embedded in most smartphones and tablet devices nowadays, which have many attractive properties such as low cost, small size, and low power consumption.

The associate editor coordinating the review of this manuscript and approving it for publication was Giancarlo Fortino.

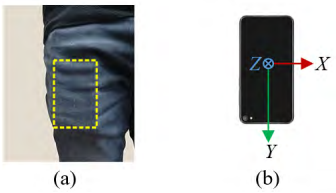

FIGURE 1. Smartphone placement and orientation. (a) Common location for carrying a smartphone. (b) Smartphone's initial orientation in this paper.

MEMS IMU-based localization is an infrastructure-free technique to track a person's location in indoor environments. Such technique works well in the non-line-of-sight (NLOS) conditions, where the wireless signal-based localization may be greatly affected. However, the conventional strap-down inertial navigation system (SINS) performs position update by numerical integration, which makes that any small error will accumulate over time. This mechanism requires high-accuracy inertial sensors, whereas the smartphone's built-in sensors cannot meet the accuracy requirement. Therefore, the main challenge in developing a smartphone-based SINS is to ensure a sufficient accuracy.

Smartphone-based indoor LBS have gained increasing research attention in the mobile application market [18]. There are many advantages of using smartphone for indoor localization: (1) as a ubiquitous portable electronic device, smartphone provides a promising platform for LBS; (2) it requires no external infrastructure and environmental information (e.g., radio fingerprint map); (3) it accords with people's established habits due to its widespread use in outdoor localization applications. Chen et al. proposed an accurate peer-assisted sound mark localization system based on smartphone, which does not require prior infrastructure or a fingerprint map [19]. However, on the one hand, online localization of landmarks is a difficult task, and the algorithm works well only if the locations of landmarks are determined in advance; on the other hand, sound marks can only be used to perform audio ranging when they are stationary.

Pedestrian dead reckoning (PDR) has become one of the popular techniques for smart device-based localization [20]. When using the low-cost MEMS inertial sensors embedded in smartphones, the error rate of a PDR system is lower than that of a pure SINS. The advantages of PDR technique are the flexible sensor placement and low requirement for sensor accuracy. Several researchers have studied the PDR technique based on handheld smartphones. In our study, smartphone is placed in the front pocket of pedestrian's pants, as illustrated in Fig. 1, which is the most common location for carrying a phone [21]. This paper aims to develop a novel PDR algorithm for indoor applications, by using the inertial sensors and magnetometer embedded in a standard off-the-shelf smartphone. The feasibility and validity of the smartphone-based PDR algorithm is verified through offline implementation with extensive experiments.

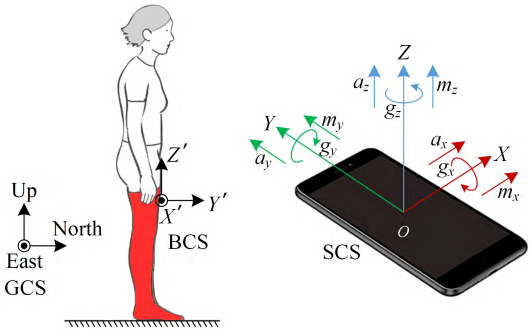

FIGURE 2. Illustration of smartphone (relative to the device), body (relative to the thigh), and global (relative to the earth) coordinate systems.

II. SENSOR CALIBRATION AND INITIAL ALIGNMENT

In this section, we give a brief description of the involved coordinate systems, the sensor error calibration, and the system initial alignment.

A. COORDINATE SYSTEMS

In the developed PDR system, three coordinate systems are established, i.e., a global coordinate system (GCS), a body coordinate system (BCS), and a phone coordinate system (SCS), which are shown in Fig. 2 and defined as follows.

1) The GCS is fixed to the earth's surface with its three axes pointing to the east, north, and up directions respectively, which is usually termed as east-north-up (ENU) coordinates;
2) The BCS is fixed to the user's body segment and denoted as $X'Y'Z'$, with its three axes pointing to the right, forward, and upward directions, respectively;
3) The SCS is fixed to the pocket-worn smartphone and denoted as XYZ, with its three axes parallel to the built-in sensor's axes.

B. SENSOR CALIBRATION

System accuracy can be improved by sensor calibration. The errors of accelerometer and gyroscope can be modeled as

$$\begin{cases} \tilde{\boldsymbol{a}}_t = \boldsymbol{K}_a(\boldsymbol{a}_t + \boldsymbol{g}) + \boldsymbol{b}_a + \boldsymbol{v}_a \\ \tilde{\boldsymbol{\omega}}_t = \boldsymbol{K}_\omega \boldsymbol{\omega}_t + \boldsymbol{b}_\omega + \boldsymbol{v}_\omega \end{cases} \tag{1}$$

where t is the sampling time, $\tilde{\boldsymbol{a}}_t$ is the measured acceleration, $\boldsymbol{a}_t$ is the actual value of acceleration without gravity, and $\boldsymbol{g}$ is the gravitational acceleration; $\boldsymbol{K}_a$ is the accelerometer scale factor, $\boldsymbol{b}_a$ is the accelerometer bias, and $\boldsymbol{v}_a$ is the accelerometer noise. Similarly, $\tilde{\boldsymbol{\omega}}_t$ and $\boldsymbol{\omega}_t$ are the measured and true angular velocities, respectively; $\boldsymbol{K}_\omega$, $\boldsymbol{b}_\omega$, and $\boldsymbol{v}_\omega$ are the scale factor, bias, and noise of the gyroscope, respectively.

Moder et al. presented a practical and effective method for sensor calibration without using expensive equipment, and experimental results showed the benefits of using calibrated rather than raw data for PDR [22]. Among the sensor errors, gyroscope bias can be estimated for each trial. Ideally, when

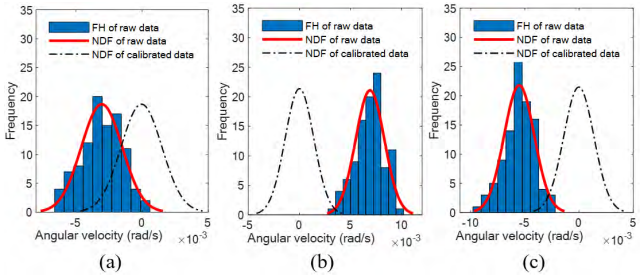

FIGURE 3. Gyroscope calibration. (a) *X*-axis data. (b) *Y*-axis data. (c) *Z*-axis data.

a sensor is stationary, the sensed angular velocities should follow a Gaussian distribution with zero mean. However, this distribution is skewed due to sensor bias. For a random trial, the frequency histogram (FH) and normal distribution fitting (NDF) of angular velocities are shown in Fig. 3.

This paper mainly focuses on the magnetometer calibration, which has a significant influence on heading estimation. A calibration method based on 3D ellipsoid fitting is used in this paper. However, as the magnetic field is easily affected by ferromagnetic materials in the surroundings, it is difficult to fully calibrate the magnetometer [23], [24]. Hence, this paper pays more attention to hard-iron calibration. In the absence of magnetic disturbances, it can be assumed that local magnetic field remains unchanged regardless of the smartphone's orientation. When rotating the smartphone in 3D space, the magnetic field vectors measured by the magnetometer should form a sphere, with a radius equal to the magnitude of local geomagnetic field. In practical applications, due to the hard- and soft-iron errors, the ideal sphere is distorted to an ellipsoid. The errors can be estimated through the ellipsoid equation expressed as

$$K_x^2(\tilde{m}_x - e_x)^2 + K_y^2(\tilde{m}_y - e_y)^2 + K_z^2(\tilde{m}_z - e_z)^2 = R^2 \tag{2}$$

where R is the norm of the local magnetic field; $\tilde{m}_x$, $\tilde{m}_y$, and $\tilde{m}_z$ are the raw magnetometer data in SCS; e_x,e_y, and e_z are the offset caused by hard-iron distortion; K_x, K_y, and K_z are the scale factors of the magnetometer.

Fig. 4 shows the raw magnetometer data and the calibrated data by using the ellipsoid fitting method. It can be found that the center of the ellipsoid deviates from the origin of SCS due to hard-iron biases. After calibration, the formed shape approximates a sphere with sufficient accuracy. In the rest of this paper, the calibrated data are used for further processing.

C. INITIAL ALIGNMENT

As there is no restriction on the position and orientation of the phone in user's pocket, the axes of SCS are rarely parallel to that of GCS in the initial state, and the smartphone's heading is generally not coincident with the actual walking direction. To solve this problem, an initial alignment method is proposed based on multi-sensor fusion. During initial alignment, the pedestrian places a smartphone vertically in the pocket, faces north, and stands still for a while with both feet on the ground, as shown in Fig. 1 and Fig. 2.

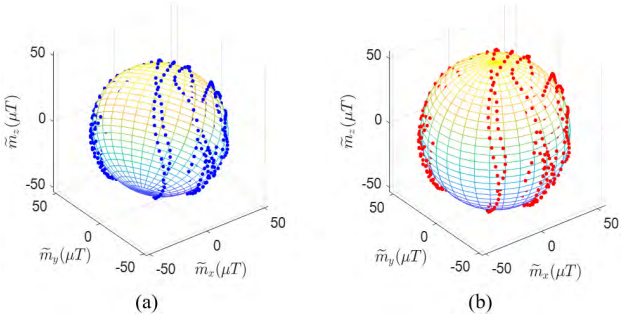

FIGURE 4. Magnetometer calibration. (a) Raw data measured by a magnetometer. (b) Calibrated data with an ellipsoid fitting method.

The initial Euler angles can be calculated as

$$\begin{cases} \phi = \text{atan}(a_y, a_z) \\ \theta = \text{atan}(a_x, -a_y s\phi - a_z c\phi) \\ \psi = \text{atan}(m_x c\theta + m_y s\theta s\phi + m_z s\theta c\phi, m_y c\phi - m_z s\phi) \end{cases} \tag{3}$$

where ϕ, θ, and ψ are the roll, pitch, and yaw angles respectively; s and c denote the sine and cosine functions; a_x, a_y, and a_z are the average values of the calibrated acceleration (with gravity); m_x, m_y, and m_z are the average values of the magnetic field density.

Although Euler angles, rotation matrices, and quaternions can equivalently represent an object's attitude, considering the so-called gimbal lock problem, the quaternion is used for attitude representation, which is defined as

$$\boldsymbol{q} = [q_0 \quad q_1 \quad q_2 \quad q_3]^T \in \Re^4 \tag{4}$$

where q_0 is the scalar part, and $[q_1 \ q_2 \ q_3]$ is vector part.

For convenience of description, three types of quaternions are introduced in our study, which are

1) ${}^G_B\boldsymbol{q}$ denotes the rotation between BCS and GCS;
2) ${}^G_S\boldsymbol{q}$ denotes the rotation between SCS and GCS;
3) ${}^B_S\boldsymbol{q}$ denotes the rotation between SCS and BCS.

Initial quaternion can be calculated from Euler angles as

$${}^G_S\boldsymbol{q}_{init} = \begin{bmatrix} q_0(0) \\ q_1(0) \\ q_2(0) \\ q_3(0) \end{bmatrix} = \begin{bmatrix} c\frac{\psi}{2}c\frac{\phi}{2}c\frac{\theta}{2} + s\frac{\psi}{2}s\frac{\phi}{2}s\frac{\theta}{2} \\ c\frac{\psi}{2}s\frac{\phi}{2}c\frac{\theta}{2} - s\frac{\psi}{2}c\frac{\phi}{2}s\frac{\theta}{2} \\ c\frac{\psi}{2}c\frac{\phi}{2}s\frac{\theta}{2} + s\frac{\psi}{2}s\frac{\phi}{2}c\frac{\theta}{2} \\ s\frac{\psi}{2}c\frac{\phi}{2}c\frac{\theta}{2} - c\frac{\psi}{2}s\frac{\phi}{2}s\frac{\theta}{2} \end{bmatrix} \tag{5}$$

In this initial condition, BCS can be designated as GCS, i.e., ${}^G_B\boldsymbol{q}_{init} \approx [1\,0\,0\,0]$. As pocket-worn smartphone is in a substantially fixed position relative to pedestrian's thigh, the quaternion ${}^B_S\boldsymbol{q}$ is assumed unchanged and can be derived as

$${}^B_S\boldsymbol{q} \approx {}^G_B\boldsymbol{q}_{init} \otimes {}^B_S\boldsymbol{q} = {}^G_S\boldsymbol{q}_{init} \tag{6}$$

Then, the thigh rotation from BCS to GCS during walking can be expressed as

$${}^G_B\boldsymbol{q} = {}^G_S\boldsymbol{q} \otimes {}^S_B\boldsymbol{q} = {}^G_S\boldsymbol{q} \otimes ({}^B_S\boldsymbol{q})^* = {}^G_S\boldsymbol{q} \otimes ({}^G_S\boldsymbol{q}_{init})^* \tag{7}$$

where the superscript * denotes complex conjugate.

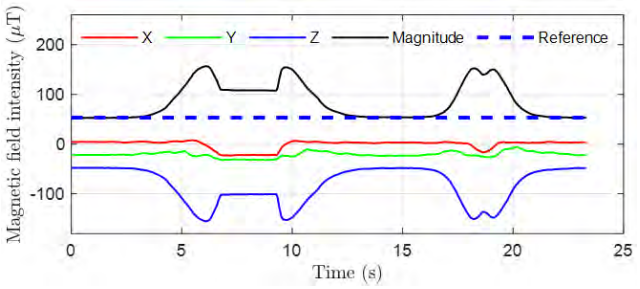

FIGURE 5. Magnetic field strength measured by the built-in magnetometer of a smartphone when the pedestrian approached an iron cabinet.

III. PEDESTRIAN DEAD RECKONING

In this section, the attitude estimation is discussed first, then the stride detection is described, and finally the stride length calculation is performed to implement the PDR.

A. ATTITUDE ESTIMATION

1) ATTITUDE ESTIMATION ALGORITHM

It is an intuitive way to estimate rotation angles by integrating the angular velocity over time. However, due to the integration operation, measurement error will accumulate and grow without bound. Sensor fusion is a promising way to improve the accuracy of attitude estimation and therefore the system's long-term stability. Many sensor fusion algorithms can be used for this purpose, such as extended Kalman filter (EKF) [25], complementary filter (CF) [26], and gradient descent based algorithm (GDA) [27]. To meet the specific requirements of the PDR system presented in our study, this paper proposes an improved data fusion algorithm based on gradient descent method.

Quaternion updating based on GDA has been described in detail by Madgwick *et al.* [27]. An important assumption in GDA is that magnetometers measure only the earth's magnetic field. However, magnetometer data are easily corrupted by magnetic interference. A segment of raw magnetometer data in indoor environment is shown in Fig. 5, where the reference value is the earth's magnetic field intensity. As is seen, the magnitude of magnetometer data fluctuates around the reference, and the disturbance of magnetic field is too severe to be ignored. In our study, magnetic interference detection (MID) is conducted to identify the accurate and usable magnetometer data, which are given by

$$update_t^{mag} = \begin{cases} 0, & \left| \left\| {}^S\boldsymbol{m}_t \right\| - m_{Earth} \right| > lim_{mag} \\ 1, & \left| \left\| {}^S\boldsymbol{m}_t \right\| - m_{Earth} \right| \le lim_{mag} \end{cases} \tag{8}$$

where $update_t^{mag}$ represents the detection result of magnetic interference, "0" means that the magnetic interference is too great for data fusion, and "1" means that the interference is within acceptable limits; ${}^S\boldsymbol{m}_t$ is the measured magnetic field vector, and $\|\cdot\|$ is the 2-norm of a vector; m_{Earth} is the intensity of the earth's magnetic field provided by the latest World Magnetic Model (WMMv2 2019) [28]; lim_{mag} is a threshold used to limit the magnetic interference.

The original GDA is improved by reducing the influence of magnetic interference on attitude estimation, as shown in Alg. 1. The improved GDA follows the gradient formulation described in [29], but introduces a switch strategy for sensor fusion mode, which ensures that the algorithm tends towards the steepest descent direction and improves the accuracy of attitude estimation. When calculating pitch and roll angles, the sensor fusion of accelerometer and gyroscope can provide sufficient accuracy, whereas fusion with magnetometer will affect the estimation accuracy. This switch can be achieved by setting the parameter $update_t^{mag}$ to 0, in which case the improved GDA works with no magnetometer data. When estimating heading angle, $update_t^{mag}$ is determined by the MID criterion given in (8), with the magnetometer data into consideration as aiding to PDR.

Algorithm 1 Improved GDA

Input: $\hat{\boldsymbol{\omega}}_t$, $\hat{\boldsymbol{a}}_t$, and $\hat{\boldsymbol{m}}_t$ are the measured angular velocity, acceleration, and magnetic field intensity, respectively; ${}^G\boldsymbol{a}$ and ${}^G\boldsymbol{m}$ are the earth's gravity and magnetic field vectors, respectively;

Output: $\hat{\boldsymbol{q}}_t$ is the updated quaternions;

${}^S\bar{\boldsymbol{\omega}}_t = \begin{bmatrix} 0 & \omega_x & \omega_y & \omega_z \end{bmatrix}$;
$f(\hat{\boldsymbol{q}}_{t-1}, \hat{\boldsymbol{a}}) = \hat{\boldsymbol{q}}_{t-1}^* \otimes {}^G\boldsymbol{a}) \otimes \hat{\boldsymbol{q}}_{t-1} - \hat{\boldsymbol{a}}$;
if $update_t^{mag}$ **then**
  $f(\hat{\boldsymbol{q}}_{t-1}, \hat{\boldsymbol{m}}) = \hat{\boldsymbol{q}}_{t-1}^* \otimes {}^G\boldsymbol{m} \otimes \hat{\boldsymbol{q}}_{t-1} - \hat{\boldsymbol{m}}_t$;
  $\nabla f(\boldsymbol{q}) = \begin{bmatrix} \boldsymbol{J}(\hat{\boldsymbol{q}}_{t-1}, \hat{\boldsymbol{a}}_t) \\ \boldsymbol{J}(\hat{\boldsymbol{q}}_{t-1}, \hat{\boldsymbol{m}}_t) \end{bmatrix}^T \begin{bmatrix} \boldsymbol{f}(\hat{\boldsymbol{q}}_{t-1}, \hat{\boldsymbol{a}}_t) \\ \boldsymbol{f}(\hat{\boldsymbol{q}}_{t-1}, \hat{\boldsymbol{m}}_t) \end{bmatrix}$;
else
  $\nabla f(\boldsymbol{q}) = \boldsymbol{J}^T(\hat{\boldsymbol{q}}_{t-1}, \hat{\boldsymbol{a}}_t) \boldsymbol{f}(\hat{\boldsymbol{q}}_{t-1}, \hat{\boldsymbol{a}}_t)$;
end if
$\dot{\boldsymbol{q}}_t = \frac{1}{2}\hat{\boldsymbol{q}}_{t-1} \otimes {}^S\bar{\boldsymbol{\omega}}_t - \beta \frac{\nabla f(\boldsymbol{q})}{\|\nabla f(\boldsymbol{q})\|}$;
$\boldsymbol{q}_t = \hat{\boldsymbol{q}}_{t-1} + \dot{\boldsymbol{q}}_t \cdot \Delta t$;
$\hat{\boldsymbol{q}}_t = \frac{\boldsymbol{q}_t}{\|\boldsymbol{q}_t\|}$.

2) ATTITUDE ESTIMATION EVALUATION

In the improved GDA, the sensor fusion mode is switched between with and without a magnetometer according to the specific attitude angles to be estimated. The concerned pitch and yaw angles can be calculated by

$$\begin{cases} \theta = \text{atan2}(2(q_0q_1 + q_2q_3), & 1 - 2(q_1^2 + q_2^2)) \\ \psi = \text{atan2}(2(q_0q_3 + q_1q_2), & 1 - 2(q_2^2 + q_3^2)) - D_{Earth} \end{cases} \tag{9}$$

where D_{Earth} denotes the earth's magnetic declination, and $\text{atan2}(y, x)$ computes the four-quadrant inverse tangent.

In (9), the orientation quaternion for calculating pitch angle θ is obtained by fusion of gyroscope and accelerometer, whereas the orientation quaternion for calculating heading angle ψ is obtained by fusion of all three types of sensors. For comparison purpose, the heading angle is estimated by three methods, i.e., the CF method, the original GDA method, and the improved GDA method. The cumulative distribution function (CDF) values of heading errors are calculated for each method, and the results are shown in Fig. 6.

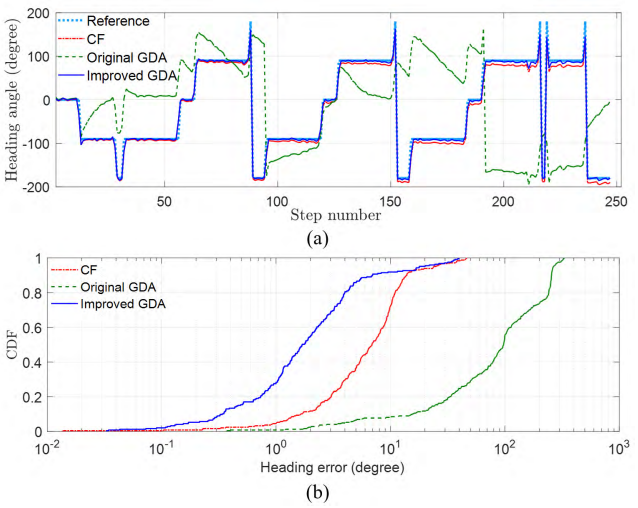

FIGURE 6. Comparison of different heading estimation methods. (a) Estimated heading angles. (b) Cumulative distribution function values of heading errors.

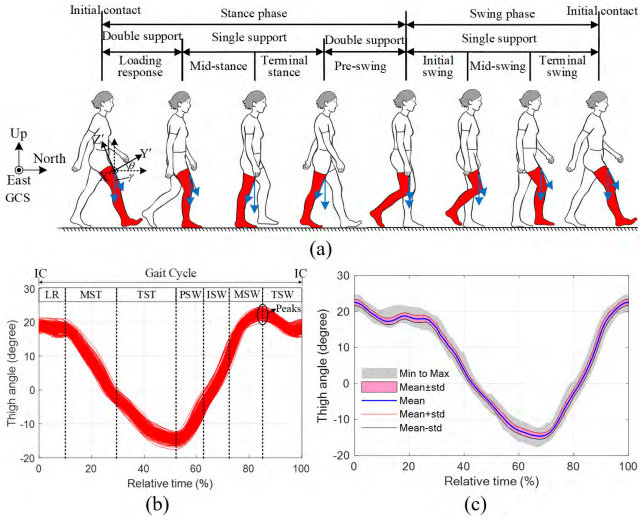

FIGURE 7. Human gait characteristics. (a) Typical gait events and gait phases. (b) Thigh angles versus gait phases in one normalized gait cycles. (c) Realigned thigh angles after dynamic time warping.

As seen in Fig. 6, the improved GDA has a 50% probability that the heading error is lower than 1.7 degrees, and an 80% probability of less than 4 degrees. The CF method has a 50% probability that the heading error is greater than 6.9 degrees, while the original GDA method has a 50% probability that the heading error is larger than 97.46 degrees. The results show that the improved GDA achieves higher accuracy than the commonly used heading estimation methods.

B. STRIDE DETECTION

1) GAIT EVENTS AND THIGH ANGLES

Combining biomechanics with pedestrian localization is shown to be a promising way to address the challenges posed by the increase of individual's autonomy using everyday objects [30]. Normally, human gait is periodic and regular, and each cycle has a sequence of ordered gait events and associated gait phases. Fig. 7(a) shows the typical gait phases during normal walking, with the initial contact (IC) specified as the start of a gait cycle. Specifically, a gait cycle can be divided into seven phases: loading response (LR), mid-stance (MST), terminal stance (TST), pre-swing (PSW), initial swing (ISW), mid-swing (MSW), and terminal swing (TSW). Armed with this information, body-worn sensors can be used to achieve gait detection. As gait motion occurs mainly in sagittal plane, gait events can be detected with respect to thigh rotation in this plane.

As shown in Fig. 7(a), thigh angle γ is defined as the angle that the thigh swings away from vertical. As is seen, the thigh angle γ reflects thigh swing more visibly than the pitch angle θ that defined as the rotation angle around the X'-axis of BCS from horizontal, although there exists $\theta{=}\gamma$. Fig. 7(b) shows the thigh angles after linear scaling over 300 gait cycles. In general, the sign of angle γ depends on the rotation direction of thigh, as defined in the following.

1) $\gamma = 0$ when the thigh is approximately parallel with the vertical axis of GCS;
2) $\gamma > 0$ when the thigh rotates counterclockwise (CCW) around the positive X'-axis;
3) $\gamma < 0$ when the thigh rotates clockwise (CW) around the positive X'-axis.

A gait cycle is the time interval between two identical and successive events of the ipsilateral lower limb during human locomotion [31], which is termed a stride and consists of two consecutive steps. As various gait events follow each other continuously and smoothly, any event could be specified as the start of a gait cycle. In our study, a thigh angle-based method is proposed to detect the concerned gait events, and the start of a gait cycle is specified as the event when the thigh angle reaches its positive peak, rather than the IC event. Fig. 7(c) shows the realigned thigh angles after dynamic time warping (DTW) for the same 300 gait cycles. For PDR purpose, the pedestrian's position is updated periodically when the positive peaks are identified.

2) GAIT DETECTION AND STRIDE DELIMITATION

Undoubtedly, gait detection is a prerequisite for PDR. In the literature, acceleration is often used for step detection by using a peak detection method [22], [32], which is expected to provide more robust results than angular velocity. In order to suppress the noise and reduce the probability of false gait detection, low-pass filter is often applied to the acceleration signals. A segment of acceleration data containing 11 strides is processed, and the detection results are shown in Fig. 8(a). As can be seen, the peak points do not differ significantly in time interval and amplitude, and therefore it is difficult to set appropriate thresholds for accurate stride delimitation.

To address the problem of acceleration-based detection method, the proposed thigh angle-based method is adopted to delimit the continuous strides. During the detection process, each thigh angle is compared with both its previous adjacent angle and its subsequent adjacent one, and two thresholds

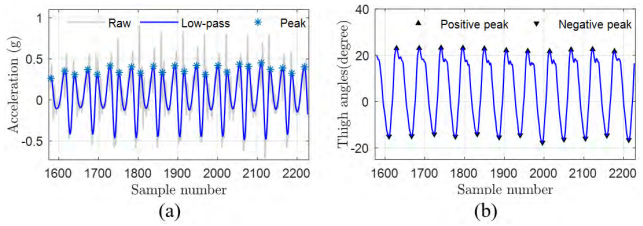

FIGURE 8. Comparison of stride detection methods using different data sources. (a) Acceleration-based detection. (b) Thigh angle-based detection.

are employed to avoid false peaks due to stand instability. As for normal human walking, there exists a time interval (e.g., at least 0.3 s) between successive peak points. Fig. 8(b) shows the detection result of the proposed algorithm, where all expected peaks of the 11 strides are detected. In addition to positive peaks that function as the onsets of strides, negative peaks are also recorded to facilitate subsequent work. The algorithm of stride detection is summarized in Alg. 2.

Algorithm 2 Stride Detection

Input: γ_t is the thigh angle at sample t; SR is the sampling rate; lim_p and lim_v are thresholds for positive and negative peak detection;

Output: (t_p, γ_p) is the location of the positive peak (stride event); (t_v, γ_v) is the location of the negative valley; (t_s, γ_s), (t_e, γ_e) are the positions of start and end events of a continuous walk, respectively;

$j = 2$; $k = 1$; $t_p(1) = 1$; $\gamma_p(1) = 0$;
for $t = 2$ to end **do**
  if $((\gamma_t > \gamma_{t-1}) \wedge (\gamma_{t+1} < \gamma_t)) \wedge (\gamma_t > lim_p)$ **then**
    if $t - t_p(j-1) > 0.3 \cdot SR$ **then**
      $t_p(j) = t$; $\gamma_p(j) = \gamma_t$; $j = j + 1$;
    end if
    if $(t_b, \gamma_b) ==$ null **then**
      $t_b = t$; $\gamma_b = \gamma_t$;
    end if
  end if
  if $((\gamma_t < \gamma_{t-1}) \wedge (\gamma_{t+1} > \gamma_t)) \wedge (\gamma_t < lim_v)$ **then**
    $t_v(k) = t$; $\gamma_v(k) = \gamma_t$; $k = k + 1$;
    if $(t_b, \gamma_b) ==$ null **then**
      $t_b = t$; $\gamma_b = \gamma_t$;
    end if
  end if
end for
if t_p(end) $> t_v$(end) **then**
  $t_e = t_p$(end); $\gamma_e = \gamma_p$(end);
else
  $t_e = t_v$(end); $\gamma_e = \gamma_v$(end);
end if

To fully evaluate the thigh angle-based stride detection algorithm, the subject was asked to walk freely along a path composed of straight lines and turns. Three performance metrics are employed, i.e., sensitivity score (SS), precision score (PS), and F-score (FS), which are determined by

$$\begin{cases} SS = TP/(TP + FN) \\ PS = TP/(TP + FP) \\ FS = 2SS \cdot PS/(SS + PS) \end{cases} \tag{10}$$

where TP denotes true positives, FP denotes false positives, and FN denotes false negatives.

The proposed thigh angle-based method is compared with the commonly used acceleration-based peak detection (PD) and zero-crossing (ZC) methods. The comparison results are listed in Table 1, which shows that our method has the best overall performance in both short and long path tests.

TABLE 1. Performance values of different stride detection methods.

Test	Method	TP	FP	FN	SS (%)	PS (%)	FS (%)
Short Path (122 strides)	PD	117	13	5	95.90	90.00	92.86
	ZC	122	21	0	100.00	85.21	92.01
	Our	121	0	1	99.18	100.00	99.59
Long Path (679 strides)	PD	676	1	3	99.56	99.85	99.70
	ZC	679	13	0	100.00	98.12	99.05
	Our	679	0	0	100.00	100.00	100.00

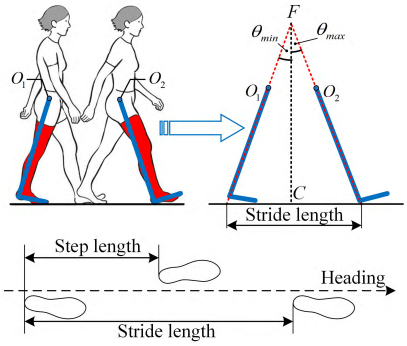

FIGURE 9. Inverted pendulum gait model for stride length estimation.

C. STRIDE LENGTH ESTIMATION

Stride length can be estimated using a gait model. An inverted pendulum model of human gait is commonly used [33]. A nonlinear stride length model was presented in [34], [35]. A step length model through first-order linear regression of pitch angle was presented in [21], [36]. This paper presents a simplified model for stride length estimation, as illustrated in Fig. 9. In this model, segment $\overrightarrow{FC}$ is parallel to the vertical direction; O_1 and O_2 are the body's center of mass (COM) at the beginning and end of each stride, θ_{max} and θ_{min} are the maximum (positive peak) and minimum (negative peak) thigh angles, respectively. Thus, the stride length can be calculated by

$$SL = \left|\overrightarrow{FC}\right| \cdot f(\theta) \tag{11}$$

where SL denotes the stride length, $|\cdot|$ denotes the segment length, and $f(\theta) = \tan(\theta_{max}) + \tan(-\theta_{min})$.

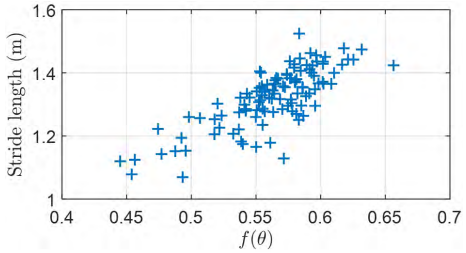

FIGURE 10. Stride length versus function $f(\theta)$ of thigh angles.

In some sense, stride length might be related to several anthropometric considerations specific to each pedestrian, such as height, leg length, foot length, knee angle, and thigh angle. As it is difficult to take all individual parameters into consideration, a trade-off is required between computational complexity and efficiency, making the estimation accuracy inevitably affected by modeling errors. Fig. 10 shows the relationship between function $f(\theta)$ and stride length SL, where each point represents a stride. Accordingly, the model for stride length estimation can be modified to

$$SL_1 = k_1 \cdot f(\theta) + b_1 \tag{12}$$

where k_1 and b_1 are the model parameters to be estimated, which approximate to 1.94 and 0.23 respectively in our study.

An acceleration-based method is proposed in [37], where the stride length is estimated by

$$SL_2 = k_2 \cdot \sqrt[3]{\sum_{t=1}^{n} \|\boldsymbol{a}_t\|/n} \tag{13}$$

where n is the number of samples in a gait cycle, and k_2 is parameter that need to be adjusted.

Inspired by the idea of complementary filtering, the models in (12) and (13) are combined with a relative weight α by

$$\widetilde{SL} = \alpha \cdot SL_1 + (1-\alpha) \cdot SL_2 \tag{14}$$

D. LOCATION ESTIMATION

The proposed PDR is a relative positioning solution, which is implemented by propagating pedestrian's position based on the estimated walking distance and direction on a 2D plane. Thus, with known previous position as well as stride length and heading angle of the current stride, the latest position can be calculated by

$$\boldsymbol{P}_t = \begin{bmatrix} P_t^N \\ P_t^E \end{bmatrix} = \underbrace{\begin{bmatrix} P_{t-1}^N \\ P_{t-1}^E \end{bmatrix}}_{\boldsymbol{P}_{t-1}} + \widetilde{SL}_t \begin{bmatrix} \cos(\psi_t) \\ \sin(\psi_t) \end{bmatrix} \tag{15}$$

where $\boldsymbol{P}_t$ and $\boldsymbol{P}_{t-1}$ are the current and previous positions, respectively; P_t^N and P_t^E are the displacements in north and east directions of GCS from initial position, respectively.

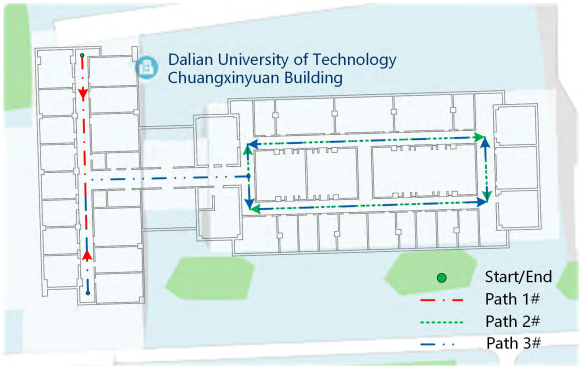

FIGURE 11. Floor plan and walking path.

IV. EXPERIMENT AND RESULT

In this section, the experimental setup is described first, then the experimental results are presented, and finally some discussions are made on the experimental results.

A. EXPERIMENTAL SETUP

To evaluate the proposed smartphone-based PDR system, experiments were carried out in a typical indoor environment. The iPhone 8 plus from Apple Inc. is used for data collection, which is equipped with a six-DOF IMU and a three-axis magnetometer, with a weight of 202g and dimensions of 158.4 mm × 78.1 mm × 7.5 mm. The experimental data were sampled at a frequency of 50 Hz. The sensed data flow was first stored in the smartphone's memory, and then processed off-line using MATLAB (MathWorks, Natick, MA, USA).

Three types of reference paths were planned, as shown in Fig. 11. The subjects were asked to place the smartphone in a front pocket of their pants and walk/turn freely along the predefined paths. Before each walking, the pedestrian was instructed to face north and stand still for a short while (e.g., about 5 s), to perform the sensor calibration and initial alignment as discussed in Section II. As only the walking on horizontal plane is considered in this paper, the vertical displacement is assumed to be zero.

B. EXPERIMENTAL RESULTS

To facilitate the analysis of experimental results, the initial position is set to the origin of GCS, and the initial direction is aligned with the X-axis of GCS. As our study focuses on relative indoor localization only, the estimation of absolute initial position is beyond the scope of this paper.

1) STRAIGHT-LINE WALKING PATH

The walking experiment was first carried out along a straight-line path (Path 1#) of 37.80 m long. One subject participated in this experiment, and was asked to walk forward (trial 1#) and backward (trial 2#) at a normal pace. Each trial was repeated three times. Fig. 12 shows the walking trajectories estimated by our method, together with a partial enlarged view of the final positions.

TABLE 2. Experimental results of straight-line walking (Path 1#).

Trial		Duration	Stride frequency	Average stride length	Stride count		Distance		Final position		Final position error	
					Measurement	Truth	Measurement	Reference	Measurement	Reference	Absolute	Relative
1#	1st	31.50 s	55 stride/min	1.31 m	**28**	29	36.78 m	37.80 m	(36.68, -0.10)	(37.8, 0)	1.12 m	**3.05%**
	2nd	30.58 s	57 stride/min	1.31 m	29	29	38.08 m	37.80 m	(37.99, -0.18)	(37.8, 0)	0.26 m	0.68%
	3rd	30.80 s	56 stride/min	1.31 m	29	29	37.89 m	37.80 m	(37.78, -0.43)	(37.8, 0)	0.43 m	1.13%
2#	1st	31.12 s	56 stride/min	1.31 m	29	29	37.85 m	37.80 m	(0.04, -0.15)	(0, 0)	0.16 m	0.42%
	2nd	31.54 s	55 stride/min	1.30 m	29	29	37.66 m	37.80 m	(0.26, -1.44)	(0, 0)	1.46 m	**3.88%**
	3rd	30.98 s	56 stride/min	1.30 m	29	29	37.70 m	37.80 m	(0.22, 0.01)	(0, 0)	0.22 m	**0.58%**
Mean		31.10 s	56 stride/min	1.31 m	29	29	37.66 m	-	-	-	**0.61 m**	**1.62%**

TABLE 3. Experimental results of closed rectangular walking (Path 2#).

Trial	Duration	Stride frequency	Average stride length	Stride count		Distance		Final position		Final position error	
				Measurement	Truth	Measurement	Reference	Measurement	Reference	Absolute	Relative
1st	71.00 s	58 stride/min	1.32 m	69	69	90.89 m	92.46 m	(0.42, -0.40)	(0, 0)	0.58 m	**0.64%**
2nd	69.64 s	59 stride/min	1.33 m	68	68	90.44 m	92.46 m	(0.04, -1.14)	(0, 0)	1.14 m	**1.26%**
3rd	70.74 s	59 stride/min	1.31 m	69	69	90.45 m	92.46 m	(-0.54, 0.74)	(0, 0)	0.92 m	1.02%
4th	78.14 s	55 stride/min	1.27 m	71	71	90.32 m	92.46 m	(0.63, -0.61)	(0, 0)	0.88 m	0.95%
5th	77.46 s	55 stride/min	1.27 m	71	71	90.13 m	92.46 m	(0.57, -0.85)	(0, 0)	1.02 m	1.13%
Mean	73.40 s	57 stride/min	1.30 m	70	70	90.45 m	-	-	-	**0.91 m**	**1.00%**

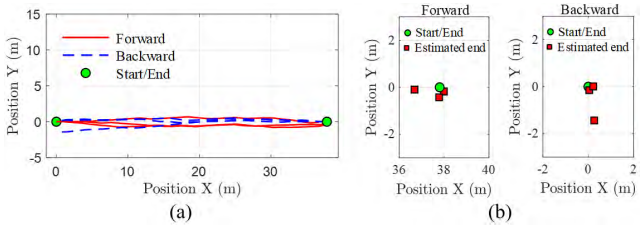

FIGURE 12. Straight-line walking along Path 1#. (a) Estimated walking trajectories. (b) Partial enlarged view of final positions.

The detailed experimental results are listed in Table 2. Statistical analysis of the experimental results shows that the estimated distance is 37.66±0.46 m, and the distance error is −0.14±0.46 m, which means that the average of estimated walking distances is less than the predefined actual distance. The absolute position error is 0.61±0.55 m. As the Path 1# is not a closed trajectory, the relative position error is defined as the ratio of absolute position error to reference distance. Thus, the maximum, minimum, and mean relative position errors are 3.88%, 0.58%, and 1.62% respectively.

2) CLOSED RECTANGULAR WALKING PATH

For a rich data collection, five subjects participated in this experiment, and each subject was requested to walk along a closed rectangular path (Path 2#) once. This path has four turns with a total distance of 92.46 m. During walking, the subjects were not instructed to turn exactly the same shape of the trajectory, but to turn slowly in their own comfortable way. Therefore, the estimated trajectories have no strict right angles at the corners, as shown in Fig. 13(a). Total number of actual strides is 348 and associated walking distance is 452 m, which indicates that the actual walking distance is shorter than the planned path length. Detailed experimental results are given in Table 3. As is shown, the absolute position error is 0.91±0.21 m, while the maximum, minimum, and mean relative position errors are 1.26%, 0.64%, and 1.00% respectively. The partial enlarged view of final positions is shown in Fig. 14(a).

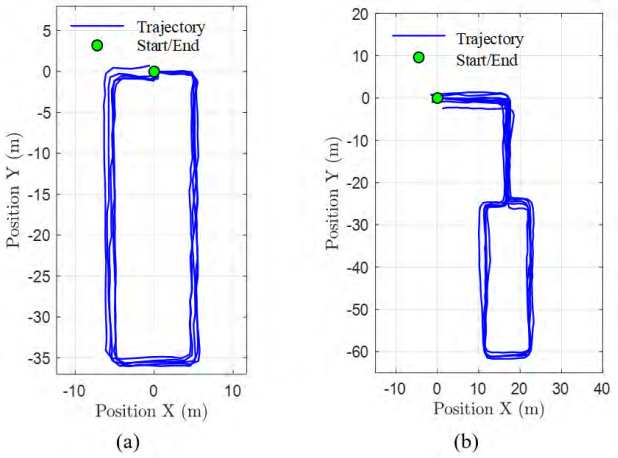

FIGURE 13. Estimated trajectories of closed-loop walking. (a) Rectangular walking along Path 2#. (b) Complex walking along Path 3#.

3) CLOSED COMPLEX WALKING PATH

To further evaluate the algorithm, the five subjects were asked to walk along a closed complex path (Path 3#), which is 175.26 m long and includes eight turns. The subjects not only passed through the busiest hallway of the floor, but also approached a power control room, an elevator, and other electro-magnetic interference environments. The estimated trajectories are shown in Fig. 13(b). Total number of actual strides is 664 and associated walking distance is 858 m. More detailed experimental data are given in Table 4. As is seen, the absolute position error is 1.57±0.95 m, while the maximum, minimum, and mean relative position errors are 1.60%, 0.06%, and 0.92% respectively. The partial enlarged view of final positions is shown in Fig. 14(b).

TABLE 4. Experimental results of closed complex walking (Path 3#).

Trial	Duration	Stride frequency	Average stride length	Stride count		Distance		Final position		Final position error	
				Measurement	Truth	Measurement	Reference	Measurement	Reference	Absolute	Relative
1st	136.90 s	57 stride/min	1.32 m	130	130	171.29 m	175.26 m	(1.15, -2.49)	(0, 0)	2.74 m	**1.60%**
2nd	140.74 s	56 stride/min	1.29 m	132	132	169.81 m	175.26 m	(-1.71, 0.68)	(0, 0)	1.84 m	1.08%
3rd	142.60 s	56 stride/min	1.27 m	133	133	169.24 m	175.26 m	(-1.39, -0.99)	(0, 0)	1.71 m	1.01%
4th	146.70 s	56 stride/min	1.27 m	137	137	173.33 m	175.26 m	(-1.38, -0.40)	(0, 0)	1.44 m	0.83%
5th	139.14 s	57 stride/min	1.32 m	132	132	174.70 m	175.26 m	(-0.10, 0.05)	(0, 0)	0.11 m	**0.06%**
Mean	141.22 s	56 stride/min	1.29 m	133	133	171.67 m	-	-	-	**1.57 m**	**0.92%**

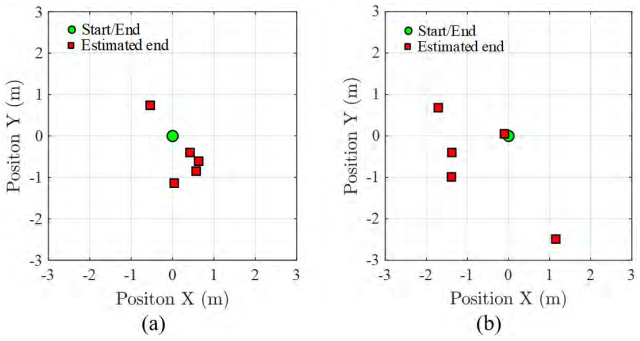

FIGURE 14. Partial enlarged view of return positions of closed-loop walking. (a) Rectangular walking along Path 2#. (b) Complex walking along Path 3#.

C. DISCUSSION

As shown in Table 2, the 1st walking of trial 1# has a miss-detection of stride. This is because the subject made some gait adjustments at the end of walking, trying to arrive at the end point accurately, which makes the final stride too small in magnitude to be detected. Stride miss-detection results in an omission of position update and ultimately a larger position error, i.e., 3.05%. However, pedestrians rarely engage in this behavior during normal walking. The 2nd walking of trial 2# has a position error as high as 3.88%. As seen in Fig. 12, heading drift is the main error source, since there exists little distance error, which in turn proves that the stride length model works well for straight-line walking.

According to the experimental results of the closed paths shown in Fig. 13, it is found that pedestrians barely walked exactly along the predefined path. In other words, pedestrians intended to walk along the path, but the actual walking trajectory could not completely coincide with the path due to the sideways swing of the body, which makes that limited ground truth is available. Therefore, return position error is chosen as a performance metric. Although the results of walking along Path 3# have higher absolute position errors than that of Path 2#, their relative position errors are comparable. This indicates that our indoor positioning algorithm is stable, as the relative position error does not diverge much with the increase of walking distance.

It is difficult to directly compare the performance values from the literature, due to the different experimental setups and performance metrics. Even though, our experimental results are comparable to or better than some of the best results reported in the literature.

1) With external aiding, the position error was bounded within 1-2 m during the walking test in [15], whereas the estimated trajectories in our study fit better with the ground truth, especially for short-term walking. A relative return position errors of 1.40% was reported in [35] along a rectangular walking trajectory, which was greater than 1.00% obtained in our study.
2) Without external aiding, the average position error of 1.18 m was reported in [18], whereas our results fit better with the ground truth without notable deviation from the walking trajectory. The relative position errors of straight-line and rectangular trajectories were 1.25% and 0.60% respectively in [36], with each experiment performed once, whereas the performance values in several of our experiments are comparable to or better than that reported in this literature.

V. CONCLUSION AND FUTURE WORK

This paper implements a self-contained PDR system based on a pocket-worn smartphone, by using the inertial sensor and magnetometer embedded in the smartphone. Three key components are involved in the PDR process, i.e., attitude estimation, stride detection, and stride length estimation. To reduce the heading drift, the original GDA is improved by accounting for the influence of magnetic interference. A thigh angle-based method is proposed for stride detection, which performs better than the commonly used acceleration-based detection method. Finally, a stride length model is proposed in a complementary way by fusing both thigh angle and acceleration. The experimental results highlight the potential use of such system in indoor localization.

In future work, we will consider the fusion of absolute positioning method in indoor environments, which can be image-based, Wi-Fi-based, Bluetooth-based, etc. Besides, we will consider the online implementation of PDR algorithm by using the mobile computing resources, which involves the evaluation of real-time performance and computational complexity, together with the construction of high-precision map and the power consumption of mobile devices.

REFERENCES

[1] G. Aloi, G. Caliciuri, G. Fortino, R. Fortino, P. Pace, W. Russo, and C. Savaglio, "Enabling IoT interoperability through opportunistic smartphone-based mobile gateways," *J. Netw. Comput. Appl.*, vol. 81, pp. 74–84, Mar. 2017.

[2] H. Yang, R. Zhang, J. Bordoy, F. Höflinger, W. Li, C. Schindelhauer, and L. Reindl, "Smartphone-based indoor localization system using inertial sensor and acoustic transmitter/receiver," *IEEE Sensors J.*, vol. 16, no. 22, pp. 8051–8061, Nov. 2016.
[3] S. Tomažič, D. Dovžan, and I. Škrjanc, "Confidence-interval-fuzzy-model-based indoor localization," *IEEE Trans. Ind. Electron.*, vol. 66, no. 3, pp. 2015–2024, Mar. 2019.
[4] L. Pei, D. Liu, D. Zou, R. L. F. Choy, Y. Chen, and Z. He, "Optimal heading estimation based multidimensional particle filter for pedestrian indoor positioning," *IEEE Access*, vol. 6, pp. 49705–49720, 2018.
[5] H. Zhao, Z. Wang, Q. Gao, M. M. Hassan, and A. Alelaiwi, "Smooth estimation of human foot motion for zero-velocity-update-aided inertial pedestrian navigation system," *Sensor Rev.*, vol. 35, no. 4, pp. 389–400, May 2015.
[6] R. Gravina, P. Alinia, H. Ghasemzadeh, and G. Fortino, "Multi-sensor fusion in body sensor networks: State-of-the-art and research challenges," *Inf. Fusion*, vol. 35, pp. 68–80, May 2017.
[7] G. Fortino, S. Galzarano, R. Gravina, and W. Li, "A framework for collaborative computing and multi-sensor data fusion in body sensor networks," *Inf. Fusion*, vol. 22, pp. 50–70, Mar. 2015.
[8] G. Fortino, R. Giannantonio, R. Gravina, P. Kuryloski, and R. Jafari, "Enabling effective programming and flexible management of efficient body sensor network applications," *IEEE Trans. Human–Mach. Syst.*, vol. 43, no. 1, pp. 115–133, Jan. 2013.
[9] S. Qiu, Z. Wang, H. Zhao, L. Liu, J. Li, Y. Jiang, and G. Fortino, "Body sensor network based robust gait analysis: Toward clinical and at home use," *IEEE Sensors J.*, to be published.
[10] W. Sun, M. Xue, H. Yu, H. Tang, and A. Lin, "Augmentation of fingerprints for indoor WiFi localization based on Gaussian process regression," *IEEE Trans. Veh. Technol.*, vol. 67, no. 11, pp. 10896–10905, Nov. 2018.
[11] F. Yin, Y. Zhao, F. Gunnarsson, and F. Gustafsson, "Received-signal-strength threshold optimization using Gaussian processes," *IEEE Trans. Signal Process.*, vol. 65, no. 8, pp. 2164–2177, Apr. 2017.
[12] B. Hanssens, D. Plets, E. Tanghe, C. Oestges, D. P. Gaillot, M. Liénard, T. Li, H. Steendam, L. Martens, and W. Joseph, "An indoor variance-based localization technique utilizing the UWB estimation of geometrical propagation parameters," *IEEE Trans. Antennas Propag.*, vol. 66, no. 5, pp. 2522–2533, May 2018.
[13] K. Yu, K. Wen, Y. Li, S. Zhang, and K. Zhang, "A novel NLOS mitigation algorithm for UWB localization in harsh indoor environments," *IEEE Trans. Veh. Technol.*, vol. 68, no. 1, pp. 686–699, Jan. 2019.
[14] J. J. Pomarico-Franquiz and Y. S. Shmaliy, "Accurate self-localization in RFID tag information grids using FIR filtering," *IEEE Trans Ind. Informat.*, vol. 10, no. 2, pp. 1317–1326, May 2014.
[15] V. Pasku, A. De Angelis, A. Moschitta, P. Carbone, J.-O. Nilsson, S. Dwivedi, and P. Händel, "A magnetic ranging-aided dead-reckoning positioning system for pedestrian applications," *IEEE Trans. Instrum. Meas.*, vol. 66, no. 5, pp. 953–963, May 2017.
[16] Z. Wang, H. Zhao, S. Qiu, and Q. Gao, "Stance-phase detection for ZUPT-aided foot-mounted pedestrian navigation system," *IEEE/ASME Trans. Mechatronics*, vol. 20, no. 6, pp. 3170–3181, Dec. 2015.
[17] H. Zhao, Z. Wang, S. Qiu, Y. Shen, L. Zhang, K. Tang, and G. Fortino, "Heading drift reduction for foot-mounted inertial navigation system via multi-sensor fusion and dual-gait analysis," *IEEE Sensors J.*, to be published.
[18] M. Zhang, Y. Wen, J. Chen, X. Yang, R. Gao, and H. Zhao, "Pedestrian dead-reckoning indoor localization based on OS-ELM," *IEEE Access*, vol. 6, pp. 6116–6129, 2018.
[19] H. Chen, F. Li, and Y. Wang, "SoundMark: Accurate indoor localization via peer-assisted dead reckoning," *IEEE Internet Things J.*, vol. 5, no. 6, pp. 4803–4815, Dec. 2018.
[20] F. Gu, K. Khoshelham, C. Yu, and J. Shang, "Accurate step length estimation for pedestrian dead reckoning localization using stacked autoencoders," *IEEE Trans. Instrum. Meas.*, to be published.
[21] E. M. Diaz and A. L. M. Gonzalez, "Step detector and step length estimator for an inertial pocket navigation system," in *Proc. Int. Conf. Indoor Positioning Indoor Navigat.*, Busan, South Korea, Oct. 2014, pp. 105–110.
[22] T. Moder, C. Reitbauer, M. Dorn, and M. Wieser, "Calibration of smartphone sensor data usable for pedestrian dead reckoning," in *Proc. Int. Conf. Indoor Positioning Indoor Navigat.*, Sapporo, Japan, Sep. 2017, pp. 1–8.
[23] A. Olivares, G. Ruiz-Garcia, G. Olivares, J. M. Górriz, and J. Ramirez, "Automatic determination of validity of input data used in ellipsoid fitting MARG calibration algorithms," *Sensors*, vol. 13, no. 9, pp. 11797–11817, Sep. 2013.
[24] N. Choe, H. Zhao, S. Qiu, and Y. So, "A sensor-to-segment calibration method for motion capture system based on low cost MIMU," *Measurement*, vol. 131, pp. 490–500, Jan. 2019.
[25] A. M. Sabatini, "Quaternion-based extended Kalman filter for determining orientation by inertial and magnetic sensing," *IEEE Trans. Biomed. Eng.*, vol. 53, no. 7, pp. 1346–1356, Jul. 2006.
[26] R. Mahony, T. Hamel, and J.-M. Pflimlin, "Nonlinear complementary filters on the special orthogonal group," *IEEE Trans. Autom. Control*, vol. 53, no. 5, pp. 1203–1218, Jun. 2008.
[27] S. O. H. Madgwick, A. J. L. Harrison, and R. Vaidyanathan, "Estimation of IMU and MARG orientation using a gradient descent algorithm," in *Proc. IEEE Int. Conf. Rehabil. Robot.*, Zürich, Switzerland, Jun./Jul. 2011, pp. 1–7.
[28] H. Park and K. M. Lee, "Joint estimation of camera pose, depth, deblurring, and super-resolution from a blurred image sequence," in *Proc. IEEE Int. Conf. Comput. Vis.*, Venice, Italy, Oct. 2017, pp. 4613–4621.
[29] M. Admiraal, S. Wilson, and R. Vaidyanathan, "Improved formulation of the IMU and MARG orientation gradient descent algorithm for motion tracking in human-machine interfaces," in *Proc. IEEE Int. Conf. Multisensor Fusion Integr. Intell. Syst.*, Daegu, South Korea, Nov. 2017, pp. 403–410.
[30] M. Abid, V. Renaudin, Y. Aoustin, E. Le-Carpentier, and T. Robert, "Walking gait step length asymmetry induced by handheld device," *IEEE Trans. Neural Syst. Rehabil. Eng.*, vol. 25, no. 11, pp. 2075–2083, Nov. 2017.
[31] H. Zhao, Z. Wang, S. Qiu, J. Wang, F. Xu, Z. Wang, and Y. Shen, "Adaptive gait detection based on foot-mounted inertial sensors and multi-sensor fusion," *Inf. Fusion*, vol. 52, pp. 157–166, Dec. 2019.
[32] F. Gu, K. Khoshelham, J. Shang, F. Yu, and Z. Wei, "Robust and accurate smartphone-based step counting for indoor localization," *IEEE Sensors J.*, vol. 17, no. 11, pp. 3453–3460, Jun. 2017.
[33] E. Allseits, V. Agrawal, J. Lučarević, R. Gailey, I. Gaunaurd, and C. Bennett, "A practical step length algorithm using lower limb angular velocities," *J. Biomech.*, vol. 66, pp. 137–144, Jan. 2018.
[34] Z. Chen, Q. Zhu, and Y. C. Soh, "Smartphone inertial sensor-based indoor localization and tracking with ibeacon corrections," *IEEE Trans. Ind. Informat.*, vol. 12, no. 4, pp. 1540–1549, Aug. 2016.
[35] Y. Zhou, X. Zheng, R. Chen, H. Xiong, and S. Guo, "Image-based localization aided indoor pedestrian trajectory estimation using smartphones," *Sensors*, vol. 18, no. 1, p. 258, Jan. 2018.
[36] A. Poulose, O. S. Eyobu, and D. S. Han, "An indoor position-estimation algorithm using smartphone IMU sensor data," *IEEE Access*, vol. 7, pp. 11165–11177, 2019.
[37] J. W. Kim, H. J. Jang, D. H. Hwang, and C. Park, "A step, stride and heading determination for the pedestrian navigation system," *J. Global Positioning Syst.*, vol. 3, no. 1–2, pp. 273–279, Dec. 2004.

HONGYU ZHAO (M'19) received the B.Sc., M.Sc., and Ph.D. degrees in automatic control from the Dalian University of Technology, Dalian, China, in 2007, 2009, and 2015, respectively.

She is currently a Lecturer with the School of Control Science and Engineering and a Postdoctoral Researcher with the School of Computer Science and Technology, Dalian University of Technology. Her current research interests include pedestrian navigation, indoor localization, inertial navigation and positioning, and gait analysis.

LUYAO ZHANG received the B.S. degree in automation from Henan Polytechnic University, Jiaozuo, China, in 2016. He is currently pursuing the M.S. degree with the School of Control Science and Engineering, Dalian University of Technology, Dalian, China.

His research interests include indoor localization, gait analysis, and pedestrian navigation.

SEN QIU received the B.S. and Ph.D. degrees in automatic control from the Dalian University of Technology, Dalian, China, in 2009 and 2016, respectively.

He was a Visiting Researcher with the Department of Computer Science and Electronic Engineering, University of Essex, U.K., from 2013 to 2014. He has been a Lecturer with the School of Control Science and Engineering, Dalian University of Technology, since 2016. His research interests include information fusion, body sensor networks, and pattern recognition.

ZHELONG WANG (M'04–SM'18) received the B.S. and M.S. degrees in automatic control from the Dalian University of Technology, Dalian, China, in 1996 and 1999, respectively, and the Ph.D. degree in robotics from the University of Durham, U.K., in 2003.

In 2004, he joined the School of Electronic and Information Engineering, Dalian University of Technology, where he is currently a Professor. His research interests include robotics, intelligent control, mechatronics, body sensor networks, and machine learning.

Dr. Wang received a Research Award from the Audi Foundation, in 2008, the Dalian Excellent IT Teacher Award, in 2008, and the First Prize of the Liaoning Province Natural Science Award (Academic Paper Program), in 2009. He was elected into Liaoning Province Hundred, Thousand, and Ten Thousand Talent Project, in 2009.

NING YANG received the B.S. and M.S. degrees from Shanxi University, Shanxi, China, in 2012 and 2014, respectively. She is currently pursuing the Ph.D. degree in control theory and control engineering with the School of Control Science and Engineering, Dalian University of Technology, Dalian, China.

Her research interests include body sensor networks, pattern recognition, and machine learning.

JIAN XU received the B.S. degree in physical education from Beijing Sport University, China, in 1993, and the M.S. degree in sport humanistic sociology from the Shanghai University of Sport, China, in 2000.

He is currently an Associate Professor with the Department of Physical Education, Dalian University of Technology, Dalian, China. His research interests include health promotion of sports for different groups of people and development of children's sports ability.